



# An enhanced stress resultant plasticity model for shell structures with application in sheet metal roll forming

Emin Kocbay<sup>1</sup> · Jakob Scheidl<sup>1</sup> · Fabian Schwarzinger<sup>1</sup> · Yury Vetyukov<sup>1</sup>

Received: 23 June 2023 / Accepted: 19 October 2023 / Published online: 2 December 2023  
 © The Author(s) 2023

## Abstract

The proposed Kirchhoff–Love shell stress resultant plasticity model extends a previously reported model for plates by complementing the constitutive law of elastoplasticity with membrane effects. This enhanced model is designed for bending dominant settings with small to moderate membrane forces. It is thus implemented in a purpose-built nonlinear mixed Eulerian–Lagrangian finite element scheme for the simulation of sheet metal roll forming. Numerical experiments by imposing artificial strain histories on a through-the-thickness element are conducted to test the model against previously reported stress resultant plasticity models and to validate it against the traditional continuum plasticity approach that features an integration of relations of elastoplasticity in a set of grid points distributed over the thickness. Results of actual roll forming simulations demonstrate the practicality in comparison to the computationally more expensive continuum plasticity approach.

**Keywords** Metal plasticity · Stress resultant shell plasticity · Kirchhoff–Love shell · Roll forming · Finite element analysis · Mixed Eulerian–Lagrangian formulation

## Nomenclature

### Geometry, material and numerical parameters

$L, w, h$	length, width and thickness of the metal sheet
$E, \nu$	elastic modulus and Poisson ratio of the metal sheet
$k$	yield strength
$P$	contact penalty

### Coordinates, kinematic description, differential operators and strain measures

$x, y, z$	global Cartesian coordinates of the actual configuration
$i, j, k$	global Cartesian basis
$\overset{\circ}{x}, \overset{\circ}{y}$	material coordinates of the reference configuration of the shell model
$\zeta$	material thickness coordinate in the 3D body of the shell

$\overset{\circ}{r}, r$	position vector of the reference and the actual configuration
$u, u_x, u_y, u_z$	displacement vector and its Cartesian components
$v, \dot{u}_x$	axial material transport rate and axial material velocity
$\overset{\circ}{\nabla}, \nabla$	differential operators of the reference and the actual configuration
$\mathbf{F}$	deformation gradient tensors
$\boldsymbol{\varepsilon}_{\perp}, \boldsymbol{\varepsilon}_{\perp}^e, \boldsymbol{\varepsilon}_{\perp}^p$	in-plane parts of the total strain tensor, elastic strain tensor and plastic strain tensor in the 3D body of the shell
$\mathbf{E}, \mathbf{K}$	total membrane and bending strain tensor of the shell
$\mathbf{E}^e, \mathbf{K}^e$	elastic parts of membrane and bending strain tensor of the shell
$\mathbf{E}^p, \mathbf{K}^p$	plastic parts of membrane and bending strain tensor of the shell

✉ Yury Vetyukov  
 yury.vetyukov@tuwien.ac.at

<sup>1</sup> Institute of Mechanics and Mechatronics, Technische Universität Wien, Getreidemarkt 9, Vienna 1060, Austria

### Stresses and related variables

$\boldsymbol{\sigma}, \mathbf{N}, \mathbf{M}$	tensors of stresses, membrane forces and bending moments
$I_N, I_{NM}, I_M$	invariants of the stress resultants $\mathbf{N}$ and $\mathbf{M}$

## Forming parameters and measures of the forming process

$\rho, \varphi$	roll-gap-reduction and bending angle of the profile
$R_{Li}$	resulting contact force (roll force) on lower roll $i$
$A^P, \dot{A}^P$	densities of plastic dissipation work and dissipation power

## 1 Introduction

In this paper a stress resultant shell plasticity model for metals, which is suited for bending dominant applications such as roll forming of sheet metal, is introduced. State-of-the-art finite element schemes to model elastic-plastic forming of thin sheet metal typically rely either on full 3D-continuum elements or on continuum shell elements, where the shell deformations, which obey the kinematic hypothesis of the structural theory, are imposed on the 3D-body to treat plasticity on the continuum level. This approach is accurate and widely established [1–5], but computationally expensive in general, because it requires a through-the-thickness integration of the 3D continuum elastic-plastic constitutive laws to arrive at the stress resultants and the strain energy density of the shell.

Consequently, so-called stress resultant plasticity models are developed [6–12], where the elastic-plastic constitutive laws are stated directly in the space of the stress resultants, thus rendering the through-the-thickness integration obsolete. Oftentimes, these publications make use of some variants of the Ilyushin yield criterion [6]. This criterion represents the von Mises yield surface in terms of stress resultants, meaning bending moments and membrane forces. The Ilyushin criterion is aimed at plastic limit load analysis and merely detects elastic or fully plastic states, but does not account for the gradual spreading of the plastic zone through the thickness. Crisfield [8] augmented the Ilyushin yield criterion by introducing a pseudo-hardening variable, namely the effective plastic curvature, such that the yield criterion is now able to approximate the plastification process through the thickness. Applications of Crisfield's model are available in the open literature [9, 10].

Another attempt to augment the Ilyushin yield criterion was carried out in [12] for geometrically linear plate bending, meaning only the bending moments enter the yield criterion. The evolution of the yield surface was described by means of an isotropic hardening function, which uses the dissipation work as an internal hardening variable. This isotropic hardening function was identified with the help of reference solutions of a continuum through-the-thickness element and by means of analytical solutions for simple cases like elastic-

plastic uniaxial bending. Results were convincing and in a better agreement with continuum solutions when compared to the yield criterion of [8].

To overcome certain limitations of the previously reported stress resultant plasticity models, the plate model of [12] is modified here in an effort to treat large deformation problems of Kirchhoff–Love shells. This enhanced shell stress resultant model is obtained by appropriately pairing the isotropic hardening law of [12] with the augmented yield surface proposed by Crisfield [8]. The thus derived yield criterion is still approximate, but in contrast to the plate-model of [12] features an additional account for small to moderate membrane forces. The two established stress resultant plasticity models and the novel one are put to the test in a series of numerical experiments. The comparison against reference solutions obtained with the continuum plasticity approach reveals the capabilities of the enhanced model, which, as compared to Crisfield's approach, also exhibits an improved convergence of the time integration scheme. Furthermore, the resolution of the plastification process in terms of isotropic work hardening facilitates the account for material hardening, which may be achieved by simple extension of the hardening function that is thus far limited to an elastic ideal-plastic material.

With regard to the aforementioned application of sheet metal roll forming, the model is implemented in the mixed Eulerian–Lagrangian (MEL) finite element framework proposed in [13]. While there are various publications on roll forming simulations [14, 15], most of them utilize a classical Lagrangian kinematic formulation. However, for processes featuring axially moving continua such as a moving metal sheet passing through a roll forming mill, the Lagrangian kinematic formulation is inefficient and causes numerically induced oscillations [16, 17]. An elegant way to mitigate these drawbacks is the use of the Arbitrary Lagrangian Eulerian (ALE) methods [18], where a Lagrangian step is succeeded by a Eulerian step within a time increment. ALE methods have successfully been applied in the context of roll forming [19] and, more recently, in an investigation on configurational forces in problems of sliding shells [20]. Here, the efficient mixed Eulerian–Lagrangian (MEL) kinematic description is employed [13, 21, 22], which – in contrast to more traditional variants of ALE – allows for a solution scheme that limits the Eulerian update step to the transport of plastic variables.

Actual roll forming simulations are carried out to test the proposed stress resultant plasticity model in an application oriented context and to conclude on improvements over its predecessors. The practical relevance of the enhanced model for the simulation of the roll forming process lies in its use as an auxiliary computational tool for the design and optimization of roll forming lines. It is capable of producing accurate results at significantly reduced computation time as compared to the continuum plasticity model.

## 2 Shell plasticity in the framework of the through-the-thickness integration approach

In the following, the essentials of the shell plasticity model in the framework of the usually employed through-the-thickness integration approach, are briefly recapitulated. For the sake of generality, the governing equations of the theory are all presented in invariant form.

The deformation of a Kirchhoff–Love shell is understood as a mapping between the undeformed reference configuration of the material surface and its actual deformed configuration [23, 24]. Material particles in each configuration are identified with the position vectors  $\overset{\circ}{\mathbf{r}}$  and  $\mathbf{r}$  for the reference and the actual state, respectively. Two corresponding differential operators  $\overset{\circ}{\nabla}$  and  $\nabla$  may be defined with the help of the total differential of a field quantity  $\phi$  on the surface:

$$d\phi = d\overset{\circ}{\mathbf{r}} \cdot \overset{\circ}{\nabla}\phi = d\mathbf{r} \cdot \nabla\phi. \tag{1}$$

These planar operators implicitly contain the derivatives with respect to the two material (Lagrangian) coordinates that are typically used to parametrize the surface. The gradients of  $\overset{\circ}{\mathbf{r}}$  and  $\mathbf{r}$  are the first metric tensors:

$$\overset{\circ}{\mathbf{a}} = \overset{\circ}{\nabla}\overset{\circ}{\mathbf{r}}, \quad \mathbf{a} = \nabla\mathbf{r}, \tag{2}$$

which define lengths and angles of the surface in the two configurations. In accordance with (1), the deformation gradient tensor  $\mathbf{F}$  provides a mapping between the differential line elements:

$$d\mathbf{r} = \mathbf{F} \cdot d\overset{\circ}{\mathbf{r}}, \quad \mathbf{F} = \overset{\circ}{\nabla}\mathbf{r}^T. \tag{3}$$

The bending deformation in terms of the unshearable Kirchhoff–Love theory is connected to the change of the unit normal vector to the deformed surface  $\mathbf{n}$ , which is expressed through the second metric tensor  $\mathbf{b}$ :

$$\mathbf{b} = -\nabla\mathbf{n}, \tag{4}$$

where  $\mathbf{n}$  fulfills the constraint of orthogonality  $\mathbf{a} \cdot \mathbf{n} = 0$ . The membrane and bending strain measures correspond to the change of the components of the first and second metric tensors, respectively. Their invariant forms read:

$$\mathbf{E} = \frac{1}{2} \left( \mathbf{F}^T \cdot \mathbf{F} - \overset{\circ}{\mathbf{a}} \right), \quad \mathbf{K} = \mathbf{F}^T \cdot \mathbf{b} \cdot \mathbf{F}, \tag{5}$$

where a planar reference configuration is assumed in the definition of the curvature tensor  $\mathbf{K}$ .

In terms of the through-the-thickness approach, the shell deformations are kinematically imposed on the three-dimensional continuum, which allows to resolve the elastic-plastic rate equations on the continuum level. In accordance with the Kirchhoff kinematic hypothesis, the in-plane part of the strain tensor of the 3D body  $\boldsymbol{\epsilon}_\perp$  varies linearly in thickness direction  $\zeta$ :

$$\boldsymbol{\epsilon}_\perp = \mathbf{E} - \zeta \mathbf{K}. \tag{6}$$

The now employed additive decomposition of the planar strain tensor into an elastic and a plastic part

$$\boldsymbol{\epsilon}_\perp = \boldsymbol{\epsilon}_\perp^e + \boldsymbol{\epsilon}_\perp^p \tag{7}$$

rests on the small strain assumption for  $\boldsymbol{\epsilon}_\perp$ . This prerequisite does not preclude large overall deformations, but it does require the membrane strains  $\mathbf{E}$  to remain small and the thickness coordinate to vary in a narrow range  $-h/2 \leq \zeta \leq h/2$ . An elastic-ideal plastic material behavior with constant yield strength  $k$  is assumed for simplicity and the von Mises yield criterion is adopted to distinguish elastic and elastic-plastic states with the function

$$f = \frac{3}{2} \boldsymbol{\sigma} \cdot \boldsymbol{\sigma} - \frac{1}{2} (\text{tr } \boldsymbol{\sigma})^2 \leq k^2. \tag{8}$$

Elastic states are identified by  $f < k^2$  and yield happens at  $f = k^2$ . The planar stress tensor  $\boldsymbol{\sigma}$  is connected to the elastic part of the planar strain tensor according to Hooke’s law for the plane stress assumption:

$$\boldsymbol{\sigma} = \frac{E}{1 + \nu} \boldsymbol{\epsilon}_\perp^e + \frac{E\nu}{1 - \nu^2} \overset{\circ}{\mathbf{a}} \text{tr } \boldsymbol{\epsilon}_\perp^e = {}^4\mathbb{C} \cdot \boldsymbol{\epsilon}_\perp^e, \tag{9}$$

with the elastic modulus  $E$  and the Poisson ratio  $\nu$ ; the fourth rank plane stress elasticity tensor  ${}^4\mathbb{C}$  provides a more concise representation. It is important to acknowledge the inconsistency introduced through (9) that connects the Cauchy stresses  $\boldsymbol{\sigma}$  related to the actual state to the Green type of strain measure  $\boldsymbol{\epsilon}_\perp$  related to the reference state. However, owing to the small strain assumption this subtle distinction is of little importance here [13]. The system of equations is complemented by the associated flow rule, which determines the evolution of the plastic strains and follows from the postulate of maximum plastic dissipation [25]:

$$\dot{\boldsymbol{\epsilon}}_\perp^p = \dot{\lambda} \frac{\partial f}{\partial \boldsymbol{\sigma}}, \quad \frac{\partial f}{\partial \boldsymbol{\sigma}} = 3\boldsymbol{\sigma} - \overset{\circ}{\mathbf{a}} \text{tr } \boldsymbol{\sigma}. \tag{10}$$

The consistency parameter  $\dot{\lambda} \geq 0$  is either zero (elastic state,  $\dot{\boldsymbol{\epsilon}}_\perp^p = 0$ ) or positive (elastic-plastic state,  $\dot{\boldsymbol{\epsilon}}_\perp^p \neq 0$ ). At yield the consistency condition  $\dot{f} = 0$  requires the stress state to remain on the yield surface. It is evaluated in the usual way

[25], to derive the stress-strain relation in terms of time rates for elastic-plastic states:

$$\dot{\boldsymbol{\sigma}} = \left( {}^4\mathbf{C} - \frac{{}^4\mathbf{C} \cdot \cdot \frac{\partial f}{\partial \boldsymbol{\sigma}} \frac{\partial f}{\partial \boldsymbol{\sigma}} \cdot \cdot {}^4\mathbf{C}}{\frac{\partial f}{\partial \boldsymbol{\sigma}} \cdot \cdot {}^4\mathbf{C} \cdot \cdot \frac{\partial f}{\partial \boldsymbol{\sigma}}} \right) \cdot \cdot \dot{\boldsymbol{\varepsilon}}_{\perp}. \quad (11)$$

The fourth rank tangent stiffness tensor in brackets is symmetric in consequence of the associated flow rule [26]. The strain energy density per unit reference area expressed in terms of the through-the-thickness integration approach reads:

$$U = \int_{-h/2}^{h/2} \frac{1}{2} \boldsymbol{\varepsilon}_{\perp}^e \cdot \cdot {}^4\mathbf{C} \cdot \cdot \boldsymbol{\varepsilon}_{\perp}^e d\zeta, \quad \boldsymbol{\varepsilon}_{\perp}^e = \boldsymbol{\varepsilon}_{\perp} - \boldsymbol{\varepsilon}_{\perp}^p. \quad (12)$$

Since the energy density of the shell is obtained via a thickness integration, this approach is henceforth referred to as “continuum plasticity model” or “cp-model” in short. Regarding the finite element implementation of Sect. 5, the integration with respect to  $\zeta$  is accomplished by means of a Gaussian quadrature rule with several points  $\zeta_i$  in thickness direction.

### 3 Stress resultant model of elastic-plastic Kirchhoff-Love shell for large overall deformations

In order to avoid the computationally expensive time integration of the constitutive equations of elastoplasticity in multiple points over the thickness, inherent to the cp-model discussed above, a stress resultant model to treat elastoplasticity directly in the framework of the direct approach featuring the shell as material surface is developed here. In particular, a representation of the strain energy density in terms of the elastic parts of the shell strain measures is sought:

$$U = \frac{1}{2} (A_1 (\text{tr } \mathbf{E}^e)^2 + A_2 \mathbf{E}^e \cdot \cdot \mathbf{E}^e + D_1 (\text{tr } \mathbf{K}^e)^2 + D_2 \mathbf{K}^e \cdot \cdot \mathbf{K}^e), \quad (13)$$

which stands in contrast to the definition (12) used in the through-the-thickness approach. Like in (7) the additive decomposition of shell strain components

$$\mathbf{E} = \mathbf{E}^e + \mathbf{E}^p, \quad \mathbf{K} = \mathbf{K}^e + \mathbf{K}^p \quad (14)$$

is based on the assumption of small local strains, which also justifies the particular choice of the strain energy density as a quadratic form in the elastic strain measures with the usual stiffness coefficients:  $A_1 = E\nu h/(1 - \nu^2)$ ,  $A_2 = Eh/(1 + \nu)$ ,  $D_1 = A_1 h^2/12$  and  $D_2 = A_2 h^2/12$ . The tensors of membrane and bending stress resultants follow from (13) by means of partial differentiation:

$$\mathbf{N} = \frac{\partial U}{\partial \mathbf{E}^e} = A_1 \mathring{\mathbf{a}} \text{tr } \mathbf{E}^e + A_2 \mathbf{E}^e, \quad \mathbf{M} = \frac{\partial U}{\partial \mathbf{K}^e} = D_1 \mathring{\mathbf{a}} \text{tr } \mathbf{K}^e + D_2 \mathbf{K}^e. \quad (15)$$

To close the formulation, the governing equations of plasticity in terms of these stress resultants and a small number of internal plastic variables are restated following the concept developed in [12]. It features the plastic dissipation work  $A^p$  as internal variable that governs the evolution law for the effective yield stress. This approach is based on the observation that the yield progress in a thickness element from initial yield up to limit yield (plastic hinge) resembles isotropic hardening. This phenomenon of “structural hardening” is not to be confused with actual material hardening, which is neglected here owing to the elastic-ideal plastic material law. The model proposed in [12] is limited to the geometrically linearized framework of the plate bending problem, where  $\mathbf{N}$  can be neglected and only the bending moments  $\mathbf{M}$  need to be considered. This simplification is no longer feasible in the present context of the geometrically nonlinear shell theory owing to the inherent coupling of membrane and bending forces. The enhanced stress resultant plasticity model for the Kirchhoff-Love shell to be developed in the following shall be addressed as “shell srp-model”, in contrast to the “plate srp-model” model proposed in [12].

The derivation rests upon an augmentation of the von Mises yield criterion (8), which is defined with respect to the plane stress tensor  $\boldsymbol{\sigma}$ . Provided the current state is purely elastic, it is possible to reconstruct  $\boldsymbol{\sigma}$  in terms of the stress resultants:

$$\boldsymbol{\sigma} = -\frac{12}{h^3} \mathbf{M} \zeta + \frac{1}{h} \mathbf{N}, \quad (16)$$

which can be easily verified by means of a substitution of (6) in the elasticity law (9) and comparison to the constitutive relation (15) for the stress resultants. Initial yield occurs in an elastic limit state that is first reached at an outer fiber (upper surface or lower surface of the shell) at  $\zeta = \pm h/2$ :

$$\boldsymbol{\sigma}^{\max} = \mp \frac{6}{h^2} \mathbf{M} + \frac{1}{h} \mathbf{N}. \quad (17)$$

Hence, the initial yield surface follows by substitution of (17) in (8), which is rearranged to reach the convenient representation:

$$f_0 = I_N + 2|I_{NM}| + I_M - 1, \quad (18)$$

with  $f_0 = 0$  corresponding to first yield; the absolute value of  $|I_{NM}|$  ensures positivity of the corresponding term. The scalar variables  $I_N$ ,  $I_{NM}$  and  $I_M$  are invariants of the membrane force tensor and the bending moment tensor:

$$I_N = \frac{1}{N_0^2} \left( \frac{3}{2} \mathbf{N} \cdot \cdot \mathbf{N} - \frac{1}{2} (\text{tr } \mathbf{N})^2 \right),$$

$$I_{NM} = \frac{1}{N_0 M_0} \left( \frac{3}{2} \mathbf{N} \cdot \cdot \mathbf{M} - \frac{1}{2} \text{tr } \mathbf{N} \text{ tr } \mathbf{M} \right), \tag{19}$$

$$I_M = \frac{1}{M_0^2} \left( \frac{3}{2} \mathbf{M} \cdot \cdot \mathbf{M} - \frac{1}{2} (\text{tr } \mathbf{M})^2 \right).$$

For later usage, the partial derivatives of these invariants are also provided:

$$\begin{aligned} \frac{\partial I_N}{\partial \mathbf{N}} &= \frac{1}{N_0^2} (3\mathbf{N} - \overset{\circ}{\mathbf{a}} \text{tr } \mathbf{N}), \\ \frac{\partial I_{NM}}{\partial \mathbf{N}} &= \frac{1}{N_0 M_0} \left( \frac{3}{2} \mathbf{M} - \frac{1}{2} \overset{\circ}{\mathbf{a}} \text{tr } \mathbf{M} \right), \\ \frac{\partial I_{NM}}{\partial \mathbf{M}} &= \frac{1}{N_0 M_0} \left( \frac{3}{2} \mathbf{N} - \frac{1}{2} \overset{\circ}{\mathbf{a}} \text{tr } \mathbf{N} \right), \\ \frac{\partial I_M}{\partial \mathbf{M}} &= \frac{1}{M_0^2} (3\mathbf{M} - \overset{\circ}{\mathbf{a}} \text{tr } \mathbf{M}). \end{aligned} \tag{20}$$

The expressions are normalized with respect to the membrane force  $N_0$  and the bending moment  $M_0$  that correspond to first yield under the distinguished load cases of uniaxial tension and uniaxial bending, respectively:

$$N_0 = kh, \quad M_0 = \frac{kh^2}{6}. \tag{21}$$

The yield surface of (18) describes initial yielding exactly, but is incapable of capturing the advancement of the plastic zone in the thickness element beyond that.

In an attempt to resolve this issue, the limit yield surface is considered as the second limiting case, which corresponds to the fully plastified thickness element. Lacking exact means of derivation for this case, it is assumed that the state of limit yield can be mathematically described in the same way as initial yield. Therefore, the limit yield surface is sought as a linear combination of the invariants in the form of (18) but with a-priori unknown coefficients  $a$ ,  $b$  and  $c$ :

$$f_L = aI_N + b|I_{NM}| + cI_M - 1. \tag{22}$$

Simple thought-experiments based on the general uniaxial stress state  $\mathbf{N} = N_x \mathbf{i}\mathbf{i}$  and  $\mathbf{M} = M_x \mathbf{i}\mathbf{i}$  in direction  $\mathbf{i}$  are carried out to determine these constants. In the limit state, the uniaxial stress distribution is piecewise constant and the position of the neutral fiber is offset by an amount  $\eta$  owing to the action of the tensile force  $N_x$ :

$$\sigma_x = \begin{cases} k, & -h/2 \leq \zeta < \eta \\ -k, & \eta < \zeta \leq h/2 \end{cases}, \tag{23}$$

with the neutral fiber being located at  $\zeta = \eta$ . The magnitudes of the stress resultants follow by thickness integration to:

$$\begin{aligned} N_x(\eta) &= \int_{-h/2}^{h/2} \sigma_x \, d\zeta = 2k\eta, \\ M_x(\eta) &= - \int_{-h/2}^{h/2} \zeta \sigma_x \, d\zeta = 1/4k(h^2 - 4\eta^2). \end{aligned} \tag{24}$$

These distributions are evaluated for three distinguished types of uniaxial stress states defined by:

$$\eta_1 = \frac{h}{2}, \quad \eta_2 = 0, \quad \eta_3 = \frac{h}{2\sqrt{3}}, \tag{25}$$

where the first corresponds to uniaxial tension, the second to uniaxial bending and the third to the special state, where the mixed invariant  $I_{NM}$  becomes maximal:

$$\frac{\partial I_{NM}}{\partial \eta} = 0 \Rightarrow \eta_3 = \frac{h}{2\sqrt{3}}. \tag{26}$$

Evaluation of (22) for all three cases yields a system of linear equations, with the solution:

$$a = 1, \quad b = \frac{2}{3\sqrt{3}}, \quad c = \frac{4}{9}. \tag{27}$$

The resulting limit yield surface of (22) turns out to be identical to the one proposed by Ilyushin [6]. In an effort to represent states in-between initial and limit yielding, Crisfield [8] augmented the Ilyushin yield criterion by introducing a dimensionless pseudo-hardening variable  $\gamma$  which is identified by the uniaxial bending experiment:

$$f_{Cr} = I_N + \frac{1}{\sqrt{3}\gamma} |I_{NM}| + \frac{1}{\gamma^2} I_M - 1, \quad \gamma = \frac{1}{2} (3 - e^{-4\chi^p}). \tag{28}$$

Here,  $\chi^p$  corresponds to the dimensionless effective plastic curvature that is derived from the plastic curvature tensor  $\mathbf{K}^p$ :

$$\chi^p = \frac{Eh}{3k} \sqrt{\frac{2}{3} (\mathbf{K}^p \cdot \cdot \mathbf{K}^p + (\text{tr } \mathbf{K}^p)^2)} \tag{29}$$

By comparison to (18) and (22) with constants according to (27) one can observe that for pure bending the Crisfield yield surface exactly captures the initial yield surface;  $\chi^p = 0$  and  $\gamma = 1$  as well as the limit yield surface;  $\chi^p \rightarrow \infty$  and  $\gamma = 3/2$ .

Instead of  $\gamma$ , the newly proposed model makes use of the isotropic hardening function of the dissipative work  $k_M(A^p)$  introduced for the plate srp-model developed in [12], which was identified for the uniaxial bending continuum reference

solution. This modification amounts to the replacement of  $\gamma$  in (28) with  $k_M(A^P)/M_0$ :

$$f = I_N + \frac{1}{\sqrt{3} \frac{k_M(A^P)}{M_0}} |I_{NM}| + \frac{1}{\frac{k_M^2(A^P)}{M_0^2}} I_M - 1, \quad (30)$$

where the hardening function is defined such, that it reproduces the elastic-plastic response of a plate at pure uni-axial bending:

$$k_M^2(A^P) = -\frac{1}{36} h^3 \left( 3EA^P - 3\sqrt{EA^P} \sqrt{2hk^2 + EA^P} + 2\sqrt{3}hk^2 \arctan \frac{\sqrt{EA^P}}{\sqrt{6hk^2 + 3EA^P}} \right) + \frac{h^4 k^2}{36}. \quad (31)$$

In contrast to Crisfield's approach, the dissipation work per unit surface of the shell  $A^P$  appears as additional state variable that determines the hardening behavior in terms of the evolution of the effective yield strength  $k_M^2(A^P)$ . This implementation in the spirit of work hardening not only captures initial yield ( $k_M^2 = M_0^2$ ,  $A^P = 0$ ) and limit yield ( $k_M^2 = M_L^2$ ,  $A^P \rightarrow \infty$ ) accurately for the case of pure bending, but also facilitates the additional account for actual isotropic material hardening by means of a proper augmentation of  $k_M^2(A^P)$  [12]. Moreover, the contribution of plastic membrane strains to the work hardening can be consistently accounted for in the definition of the dissipation power:

$$\dot{A}^P = \mathbf{N} \cdot \dot{\mathbf{E}}^P + \mathbf{M} \cdot \dot{\mathbf{K}}^P. \quad (32)$$

The plate srp-model and the one suggested by Crisfield lack this ability. Two associated flow rules with a single consistency parameter  $\lambda$  are stated for the plastic strain rates:

$$\dot{\mathbf{E}}^P = \lambda \frac{\partial F}{\partial \mathbf{N}}, \quad \dot{\mathbf{K}}^P = \lambda \frac{\partial F}{\partial \mathbf{M}}, \quad (33)$$

where the original yield equation  $f = 0$  has been replaced with the modified one  $F(\mathbf{N}, \mathbf{M}) = k_M^2(A^P)$ , which in terms of the stress invariants reads:

$$F = \frac{h^4 k^2 \left( |I_{NM}| + \sqrt{12I_M(1 - I_N) + I_{NM}^2} \right)^2}{432(1 - I_N)^2} = k_M^2(A^P). \quad (34)$$

The thus achieved separation of yield criterion and effective yield strength is beneficial when it comes to the evaluation of the consistency condition:

$$\dot{F} = \frac{\partial F}{\partial \mathbf{N}} \cdot \dot{\mathbf{N}} + \frac{\partial F}{\partial \mathbf{M}} \cdot \dot{\mathbf{M}} = 2k_M k'_M \dot{A}^P, \quad (35)$$

which binds the stress state to the actual yield surface in case of plastic flow. Application of the chain rule of differentiation yields:

$$\begin{aligned} \frac{\partial F}{\partial \mathbf{N}} &= \frac{\partial F}{\partial I_N} \frac{\partial I_N}{\partial \mathbf{N}} + \frac{\partial F}{\partial I_{NM}} \frac{\partial I_{NM}}{\partial \mathbf{N}}, \\ \frac{\partial F}{\partial \mathbf{M}} &= \frac{\partial F}{\partial I_M} \frac{\partial I_M}{\partial \mathbf{M}} + \frac{\partial F}{\partial I_{NM}} \frac{\partial I_{NM}}{\partial \mathbf{M}}, \end{aligned} \quad (36)$$

which, for the sake of conciseness, is not expanded further with the help of (20). Likewise, the lengthy total derivative of  $k_M^2(A^P)$  that follows from (31) is omitted. With the dissipation power given in (32), it remains to evaluate the constitutive law (15) to relate the rates of the stress and strain resultants:

$$\begin{aligned} \dot{\mathbf{N}} &= A_1 \overset{\circ}{\mathbf{a}} \operatorname{tr} \dot{\mathbf{E}}^e + A_2 \dot{\mathbf{E}}^e = \frac{\partial \mathbf{N}}{\partial \mathbf{E}^e} \cdot \cdot (\dot{\mathbf{E}} - \dot{\mathbf{E}}^P), \\ \dot{\mathbf{M}} &= D_1 \overset{\circ}{\mathbf{a}} \operatorname{tr} \dot{\mathbf{K}}^e + D_2 \dot{\mathbf{K}}^e = \frac{\partial \mathbf{M}}{\partial \mathbf{K}^e} \cdot \cdot (\dot{\mathbf{K}} - \dot{\mathbf{K}}^P), \end{aligned} \quad (37)$$

where the elastic strain rates are replaced according to the additive decomposition (7). The tensor derivatives of  $\mathbf{N}$  and  $\mathbf{M}$  with respect to the corresponding elastic strain tensors constitute two fourth order tensors that resemble the elasticity tensor  ${}^4\mathbb{C}$  of the continuum theory (9). With the rates of the stress resultants (37) as well as the dissipation power (32) written in terms of strain rates, we utilize the flow rules (33) to solve (35) for the consistency parameter:

$$\lambda = \frac{\frac{\partial F}{\partial \mathbf{N}} \cdot \cdot \frac{\partial \mathbf{N}}{\partial \mathbf{E}^e} \cdot \cdot \dot{\mathbf{E}} + \frac{\partial F}{\partial \mathbf{M}} \cdot \cdot \frac{\partial \mathbf{M}}{\partial \mathbf{K}^e} \cdot \cdot \dot{\mathbf{K}}}{\frac{\partial F}{\partial \mathbf{N}} \cdot \cdot \frac{\partial \mathbf{N}}{\partial \mathbf{E}^e} \cdot \cdot \frac{\partial F}{\partial \mathbf{N}} + \frac{\partial F}{\partial \mathbf{M}} \cdot \cdot \frac{\partial \mathbf{M}}{\partial \mathbf{K}^e} \cdot \cdot \frac{\partial F}{\partial \mathbf{M}} + 2k_M k'_M (\mathbf{N} \cdot \cdot \frac{\partial F}{\partial \mathbf{N}} + \mathbf{M} \cdot \cdot \frac{\partial F}{\partial \mathbf{M}})}. \quad (38)$$

In analogy to (11), backward substitution in (37) reveals the tangential elastic-plastic constitutive law in the framework of the stress resultant plasticity theory. The appearance of the total strain rates  $\dot{\mathbf{E}}$  and  $\dot{\mathbf{K}}$  in (38) expresses the inherent coupling of membrane and bending deformations in the elastic-plastic regime. Therefore, curvature rates will in general evoke plastic membrane strain rates according to the flow rules (33) and vice versa.

Now that all prerequisites for the implementation of a numerical solution scheme are met, the return mapping algorithm from [12] is adapted by replacing the governing equations of the original plate srp-model with the ones of the enhanced shell srp-model.

#### 4 Elastic-plastic response of a through-the-thickness element

Here, all three previously mentioned stress resultant plasticity models (Crisfield srp-model, plate srp-model, shell

srp-model) are subjected to simple load cases and are compared to the results of reference solutions obtained with the continuum plasticity model (cp-model) of Sect. 2. Specifically, different kinds of kinematic loading are imposed on a through-the-thickness element by means of a time incrementation of the membrane strain and curvature tensor:

$$\mathbf{K} = \alpha_K(t) K_{\max} (\mathbf{ii} - \nu \mathbf{jj}), \quad \mathbf{E} = \alpha_E(t) E_{\max} \mathbf{P} \cdot (\mathbf{ii} - \nu \mathbf{jj}) \cdot \mathbf{P}^T, \tag{39}$$

where  $\mathbf{i}$  and  $\mathbf{j}$  denote the in-plane Cartesian basis vectors of the element. The rotation tensor  $\mathbf{P}$  is used to adjust the relative angular alignment of the strain measures:

$$\mathbf{P} = \mathbf{P}(\Theta) = \cos \Theta (\mathbf{ii} + \mathbf{jj}) - \sin \Theta (\mathbf{ij} - \mathbf{ji}). \tag{40}$$

The primary directions coincide for  $\Theta = 0$ , in which case an uniaxial stress state in  $\mathbf{i}$ -direction is obtained in the elastic range; small additional components of membrane forces and bending moments in the orthogonal direction arise once plastic flow occurs. A multi-axial state may be enforced by  $\Theta \neq 0$ . Alternatively, a force driven approach that would allow for a direct specification of stress states could be pursued, but the deformation driven one is preferred for ease of implementation. The kinematic loading (39) is biased towards a bending dominant application (like roll forming) with the maximum amplitudes:

$$K_{\max} = 4 \frac{12M_0}{Eh^3} = \frac{8k}{Eh}, \quad E_{\max} = \frac{1}{2} \frac{N_0}{Eh} = \frac{1}{2} \frac{k}{E}, \tag{41}$$

that correspond to four-times the curvature of first yield for pure bending and just half of the membrane strains required for yielding in the state of pure tension, respectively. The actual values are controlled with the load factors  $\alpha_K$  and  $\alpha_E$  that range from zero to one and are defined as piecewise linear functions in the timespan  $0 \leq t \leq 1$ .

The rate equations of the particular plasticity models under consideration are integrated numerically with a simple explicit scheme and a sufficiently fine time discretization. The parameters of the particular numerical experiments are specified in Table 1;  $N_\zeta$  is the number of thickness integration

points that are used for the continuum plasticity model. The element with the given material parameters and thickness  $h$  is subjected to four different load histories that are stated in terms of the angle  $\Theta$  and tabulated values for the load factors  $\alpha_E$  and  $\alpha_K$ , which are interpolated linearly between the designated points  $t = \{0.0, 0.5, 1.0\}$ . Cases 1 and 2 feature a simultaneous increase of the imposed strains (41) and differ solely in the angle  $\Theta$ . The angular alignment is varied in cases 3 and 4 as well, but, more importantly, the kinematic loads are applied sequentially, i.e.: first bending then tensioning and vice versa.

The tabulated values for the load factors are indicated at the top of the respective grid lines in the corresponding graphs of Figs. 1, 2, 3 and 4 that depict the simulated time histories of the primary invariants  $I_N$  and  $I_M$ . These variables are bounded by their uniaxial limit yield values, namely:  $I_N \leq 1$  and  $I_M \leq 9/4$ . An exception is the plate stress resultant model of [12], which may be recovered from (30) by simply setting  $I_N = I_{MN} = 0$ . Hence, the membrane stress resultants do not enter the elastic-plastic constitutive of the plate srp-model in any way and the invariant  $I_N$  is unbounded in consequence thereof. Analyzing the results presented in Figs. 1 – 4, good agreement of the novel shell srp-model with the exact continuum model is observed, which in terms of  $I_M$  also poses a slight improvement over the stress resultant plasticity model of Crisfield; regarding  $I_N$ , both models are almost indistinguishable. The great importance of including the membrane forces in the plasticity model is highlighted in comparison to the plate srp-model, which produces the same purely elastic response for  $I_N$  regardless of the imposed loading. This deficiency is most pronounced for the cases 1, 2 and 4, where the corresponding graphs of the plate srp-model for  $I_N$  deviate from the others as soon as plastic flow occurs and the purely elastic regime, for which all models are equal, is left. Interestingly, the coupling of membrane and bending resultants in these cases primarily affects the distribution of the membrane forces, but its impact on the bending behavior is weak, such that the distributions for  $I_M$  remain in close proximity to the continuum reference model. In this respect case 3 of Fig. 3 is different, because the late application of the kinematic membrane loading must cause additional plas-

**Table 1** Parameters and specific load histories for the numerical experiments on the through-the-thickness element: The angle  $\Theta$  determines the angular alignment of the prescribed strain states

$E$ [N/m <sup>2</sup> ]	$\nu$	$k$ [N/m <sup>2</sup> ]	$h$ [m]	$N_\zeta$			
$2.8 \times 10^{11}$	0.3	$362 \times 10^6$	0.003	50			
load case	$\Theta$ [rad]	$\alpha_E(0)$	$\alpha_E(0.5)$	$\alpha_E(1.0)$	$\alpha_K(0)$	$\alpha_K(0.5)$	$\alpha_K(1.0)$
1	0	0.0	0.5	1.0	0.0	0.5	1.0
2	$\pi/2$	0.0	0.5	1.0	0.0	0.5	1.0
3	$\pi/4$	0.0	0.0	1.0	0.0	1.0	1.0
4	0	0.0	1.0	1.0	0.0	0.0	1.0

The time evolution of the load factors  $\alpha_E$  and  $\alpha_K$  is given by piecewise linear interpolation of the tabulated values for  $t = \{0.0, 0.5, 1.0\}$

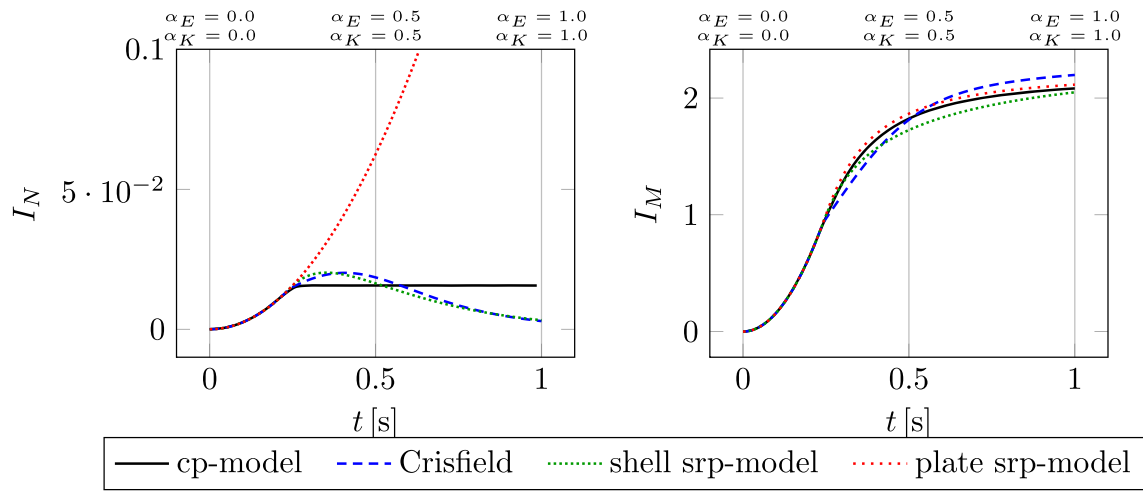


**Fig. 1** Comparison of simulation results of the through-the-thickness element between the four different plasticity models for the load case 1 of Table 1

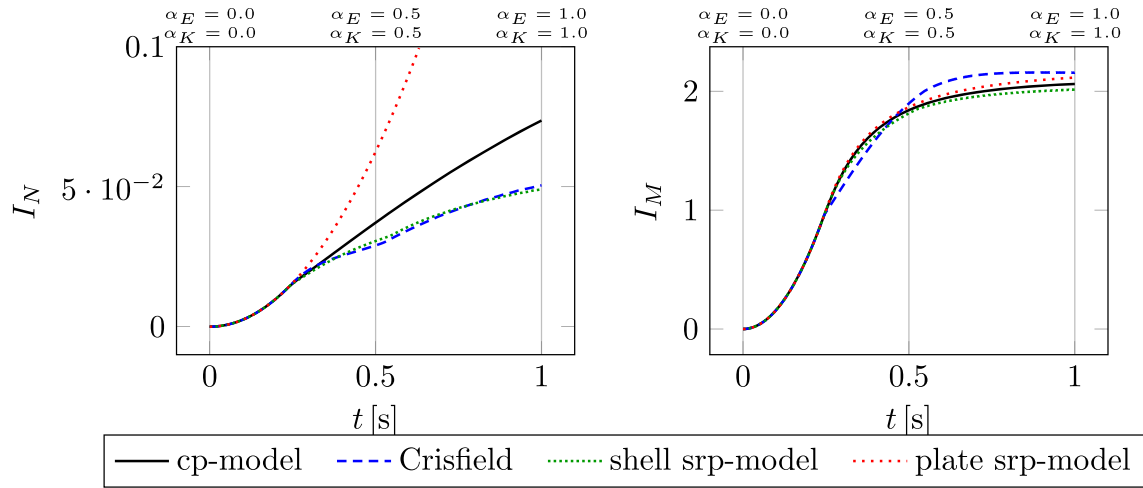


**Fig. 2** Comparison of simulation results of the through-the-thickness element between the four different plasticity models for the load case 2 of Table 1

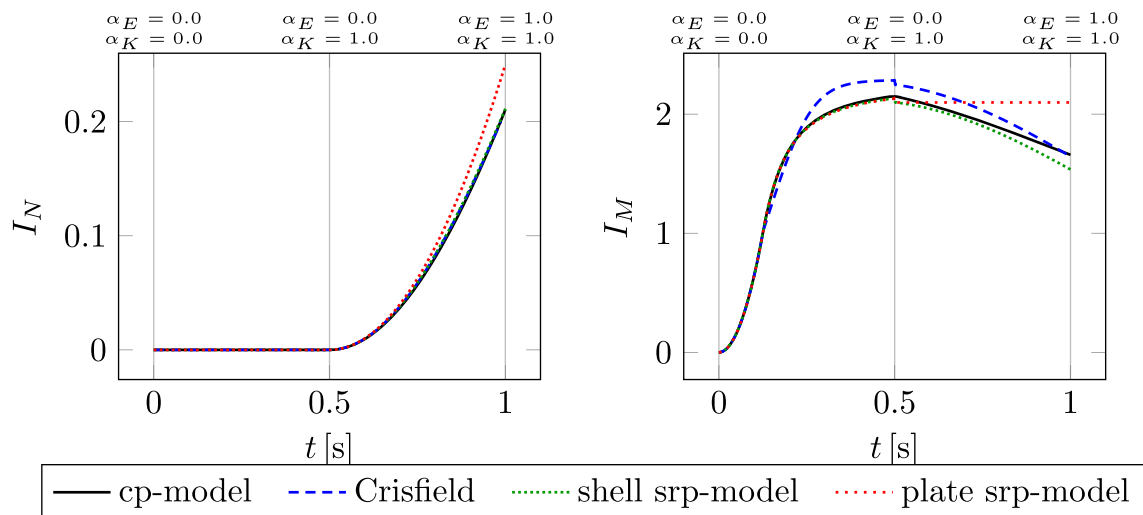


**Fig. 3** Comparison of simulation results of the through-the-thickness element between the four different plasticity models for the load case 3 of Table 1



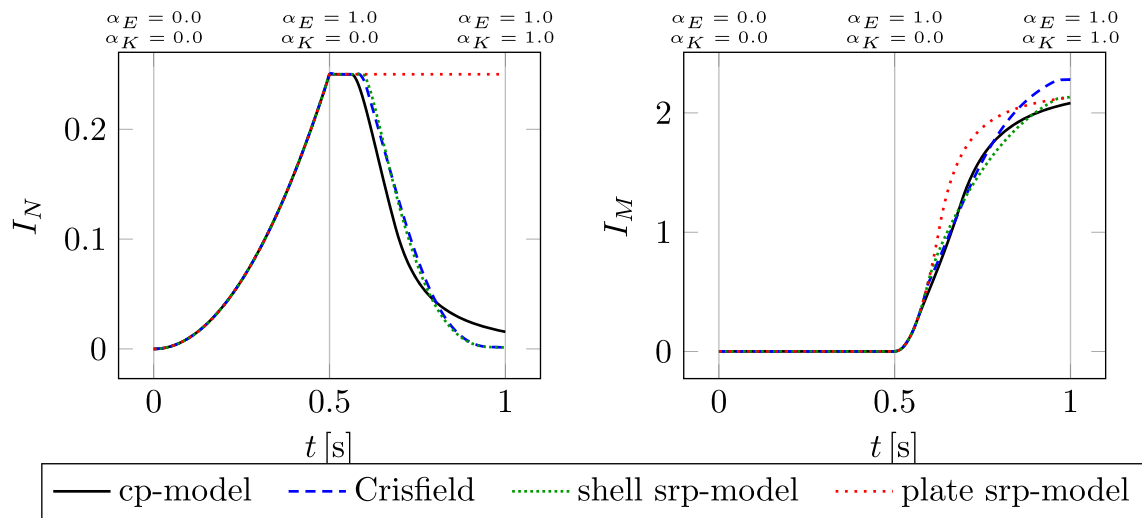


**Fig. 4** Comparison of simulation results of the through-the-thickness element between the four different plasticity models for the load case 4 of Table 1

tic curvature strains in the extended models owing to the inherent coupling best illustrated by (38). Hence, the limited capabilities of the plate srp-model show in the distribution for  $I_M$  in this special case. Evidently, the inclusion of plastic membrane strains is crucial for an accurate resolution of the stress resultants.

To investigate the essential differences of the novel shell srp-model and the one proposed by Crisfield, comparisons of the respective hardening functions  $k_M(A^P)/M_0$  and  $\gamma(\chi^P)$  are presented in Figs. 5 and 6 for all considered load cases. The values of both dimensionless hardening functions are initialized with 1, which is the limit for initial yielding. Once plastic flow occurs, the hardening functions grow towards the

limit yield value  $3/2$ . Owing to the exponential law (28), the Crisfield model always saturates very quickly. In contrast, the shell srp-model approaches the limit yield boundary slower without ever reaching it. Being based on work hardening, this model also accounts for the contribution of plastic membrane strains to the plastic work  $A^P$  that determines the progression of plastic flow in the thickness element. However, the impact is negligible in all cases, which is best illustrated by the graphs corresponding to load case 3 in Fig. 6, where the hardening function  $k_M/M_0$  remains practically constant for  $t > 0.5$  after the curvature loading has been fully applied.

The results presented so far, demonstrate the obvious advantages of the proposed shell srp-model over its prede-

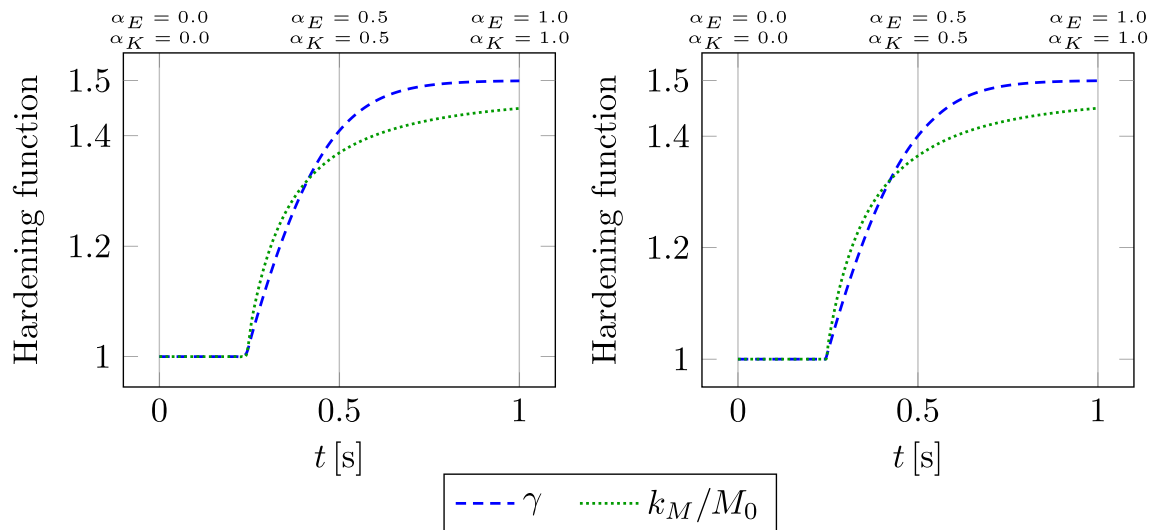


**Fig. 5** Comparison of the hardening functions for load case 1 (left) and load case 2 (right) of Table 1

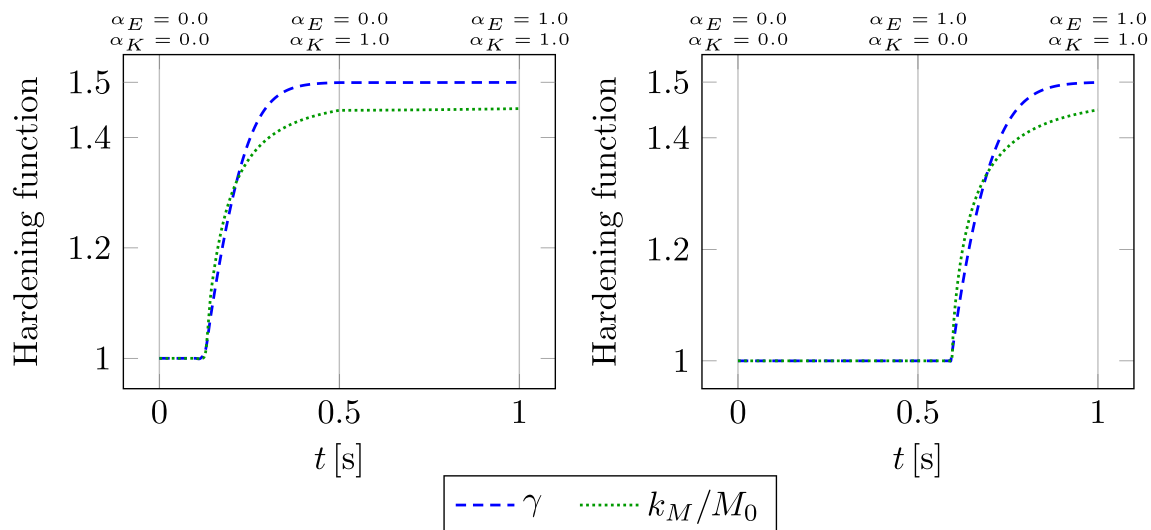


**Fig. 6** Comparison of the hardening functions for load case 3 (left) and load case 4 (right) of Table 1

cessor for the plate bending problem discussed in [12]. The primary benefits in comparison to the Crisfield stress resultant model comprise:

- modest improvements of accuracy with respect to the continuum reference solution
- the formulation in terms of a work hardening law that facilitates the inclusion of isotropic material hardening
- a significantly better convergence of the numerical time integration scheme

Regarding the last point, it is found, that the Crisfield model requires about three times more time steps than the shell srp-model in order to reach results of comparable numerical accuracy. An elaborate discussion on the time integration scheme of the Crisfield model and related limitations of [10] is available in [10]. Similar concerns regarding actual implementations of the Crisfield model were expressed in [27, 28]. Later in Sect. 7, the comparison of plasticity models by imposing the results of actual roll forming simulations on a through-the-thickness element is continued.

## 5 Mixed Eulerian–Lagrangian finite element scheme

The different plasticity models, except for the one proposed by Crisfield, are implemented in a mixed Eulerian–Lagrangian shell finite element scheme that is designed for the simulation of sheet metal roll forming. Since a detailed discussion of this program is available [13], only a brief explanation of the most essential aspects is provided, namely:

- the mixed Eulerian–Lagrangian kinematic description

- the contributions that constitute the total potential energy in the weak formulation
- frictionless contact
- the convective transport of internal plastic variables in the two-step solution procedure

Though purpose-built for the process of sheet metal forming, the simulation framework is equally applicable to certain static problems [13]; actual roll forming simulations are addressed in Sects. 6 to 8.

Since the raw material of the roll forming process is a flat metal sheet a rectangular reference configuration can now explicitly be stated:

$$\mathring{\mathbf{r}} = \mathring{x}\mathbf{i} + \mathring{y}\mathbf{j}, \quad -w/2 \leq \mathring{y} \leq w/2, \quad (42)$$

where  $\mathring{x}$  and  $\mathring{y}$  denote the Lagrangian material coordinates in axial direction and lateral (width) direction, respectively. Originally, the undeformed sheet is aligned in the  $xy$ -plane of the spatial Cartesian coordinate frame with the basis vectors  $\mathbf{i}$  and  $\mathbf{j}$ ; the complementary vector  $\mathbf{k} = \mathbf{i} \times \mathbf{j}$  points in  $z$ -direction. The lateral coordinate  $\mathring{y}$  is bounded by the total width  $w$  of the metal sheet, but the axial coordinate  $\mathring{x}$  is unbounded, because roll forming is viewed as a continuous process in a spatial control domain  $0 \leq x \leq L$ . Therefore, as forming progresses the axially moving sheet (and its material particles) will be continuously transported through this domain, which renders the purely Lagrangian perspective inefficient and suggests a coordinate transformation to a mixed set that decouples the actual deformations sustained during the forming process from the axial travel of the structure. Thus, the position vector to a material particle  $\mathbf{r}$  in the actual configuration is parametrized in a mixed coordinate

space that comprises the Eulerian axial coordinate  $x$  and the Lagrangian lateral coordinate  $\overset{\circ}{y}$ :

$$\mathbf{r} = x\mathbf{i} + (\overset{\circ}{y} + u_y)\mathbf{j} + u_z\mathbf{k}, \quad \overset{\circ}{x} = x - u_x. \tag{43}$$

Together the mixed pair  $\{x, \overset{\circ}{y}\}$  constitute a rectangular intermediate configuration of the part of the metal sheet currently enclosed by the boundaries of  $x \in [0, L]$  (active material volume). The Cartesian components of the displacement vector

$$\mathbf{u}(x, \overset{\circ}{y}, t) = u_x(x, \overset{\circ}{y}, t)\mathbf{i} + u_y(x, \overset{\circ}{y}, t)\mathbf{j} + u_z(x, \overset{\circ}{y}, t)\mathbf{k} \tag{44}$$

serve as primary unknowns. More specifically, the nodal variables of a single four-node rectangular finite element, which resides in the intermediate configuration, comprise the displacements themselves, their first derivatives and the mixed second derivative with respect to the local finite element coordinates. This choice of nodal degrees of freedom paired up with bi-cubic polynomial shape functions ensures a  $C^1$  continuous approximation of the position vector. The used finite elements are therefore an extension of the Bogner-Fox-Schmit plate elements [29, 30].

The mixed parametrization is advantageous because it enables a spatial resolution of the deformations imposed by the roll stands at given  $x$ -positions. Consequently, material particles are free to travel through the finite element mesh that is fixed in axial direction. This change of perspective necessitates a corresponding transformation of the basic kinematic relations. In particular, the material differential operator needs to be restated in terms of the partial derivatives with respect to  $x$  and  $\overset{\circ}{y}$ :

$$\overset{\circ}{\nabla} = \mathbf{i} (1 - \partial_x u_x)^{-1} \partial_x + \mathbf{j} \partial_{\overset{\circ}{y}}, \tag{45}$$

such that its application to  $\overset{\circ}{\mathbf{r}}$  with  $\overset{\circ}{x} = x - u_x$  still yields the planar unit tensor. The first coefficient represents the derivative of the Eulerian coordinate  $x$  with respect to its material counterpart  $\overset{\circ}{x}$ . Consequently, its reciprocal value determines the Jacobian determinant to transform the material area integral for the total strain energy:

$$U^\Sigma = \iint U d\overset{\circ}{x}d\overset{\circ}{y} = \int_0^L dx \int_{-w/2}^{w/2} (1 - \partial_x u_x) U d\overset{\circ}{y}, \tag{46}$$

where either (13) or (12) need to be inserted for the strain energy density  $U$  depending on the particular choice of plasticity model.

The second contribution to the total potential energy is attributed to the contact of the metal sheet with the rolls that impose the plastic bending on the initially flat metal sheet during the roll forming process. It is modelled as a frictionless contact of a solid body (metal sheet) with rigid

bodies of revolution (rolls). The assumption of frictionless contact is justified with the following reasoning:

- In reality, the interface between rolls and sheet metal is lubricated to reduce tool wear, which reduces friction and significantly complicates the identification of the friction parameters [31].
- Friction seems to have no significant impact on resulting geometry and contact normal forces [15, 31, 32].

The penalty-regularization method is employed to state the contact potential as

$$V^\Sigma = \int_0^L dx \int_{-w/2}^{w/2} (1 - \partial_x u_x) \frac{1}{2} P \gamma^2 d\overset{\circ}{y}, \tag{47}$$

with a large factor  $P$  to penalize any penetration  $\gamma \geq 0$  of the metal sheet into the roll surface; details are provided in [13]. The sum of  $U^\Sigma$  and  $V^\Sigma$  constitutes the total potential energy, which is minimized numerically to compute a quasistatic equilibrium state in the first phase of the transient simulation procedure.

Since the inner variables that identify the plastic state are strictly attached to the material particles, their flow through the Eulerian–Lagrangian finite element mesh in axial direction must be rigorously accounted for. This is done by means of solving an advection equation, which constitutes the second (Eulerian) step of the solution scheme and concludes the time increment. A forward in time backwards in space finite difference method is used to perform the incremental time integration of this equation; its implementation in the finite element scheme is discussed in [13].

## 6 Roll forming simulation for a single roll stand

In this section the enhanced shell srp-model is tested in an actual roll forming simulation with a single roll stand and its response is compared to corresponding simulations conducted with the plate srp-model of [12] and the continuum plasticity model. The same assumptions (rigid rolls, frictionless contact etc.) and simulation procedure as described in [13] is followed, which features the mixed Eulerian–Lagrangian finite element scheme outlined in Sect. 5

A control domain  $0 \leq x \leq 0.8$  m with one roll stand acting at  $x = 0.4$  m is considered, with simulation parameters according to Table 2; an axial mesh refinement (with  $N_x$  elements) such, that the elements at the contact region are half the size of the elements in the outer regions is employed. The edge at  $x = 0$  corresponds to a fully (in-plane and out-of-plane) clamped edge with material particles flowing through at the constant transport rate  $v$ . The final (steady state) con-

**Table 2** Default parameters of the simulation model with one roll stand

Geometry			Material			
$L$ [m]	$w$ [m]	$h$ [m]	$E$ [N/m <sup>2</sup> ]	$\nu$	$k$ [N/m <sup>2</sup> ]	
0.8	0.1	0.003	$2.08 \times 10^{11}$	0.3	$362 \times 10^6$	
Forming	Transport		Numerical			
$\rho$ [m]	$v$ [m/s]	$\Delta t$ [s]	$N_x$	$N_y$	$N_z$	$P$ [N/m <sup>3</sup> ]
0.004	0.8	0.005	26	10	8	$1 \times 10^{13}$

figuration with a cross-sectional view of the roll gap in the center is depicted in Fig. 7.

It visualizes the symmetrical roll profiles and also shows the forming angle  $\varphi$  as well as the roll-gap-reduction parameter  $\rho$ . The latter is used to position the rolls vertically by means of a symmetrical shift of  $\rho/2$  towards each other and the angle  $\varphi$  corresponds to the tangential direction at the end of the cross section. As postprocessing variables the resulting contact force acting on the lower rolls  $R_L$  and the bending angle  $\varphi(x = 0.6 \text{ m})$  are viewed. The angle is evaluated at this particular x-coordinate because the forming angle of an endless profile is best approximated about halfway between the roll-stand and the free end, i.e.: sufficiently far away from the rolls and the right boundary. A parameter study for varying roll-gap-reduction  $\rho$  is carried out and the resulting force  $R_L$  and the bending angle  $\varphi(x = 0.6 \text{ m})$  are plotted in Fig. 8. Evidently, the results produced by the proposed shell srp-model are mostly in line with the ones of the reference computation with the cp-model.

The good correspondence of all models regarding the bending angle is owed to the fact that the shape of the final cross section is primarily determined by the kinematically imposed roll profiles. However, the force distribution obtained for the plate srp-model deviates significantly, which can be attributed to the neglect of the membrane forces in the elastic-plastic constitutive law. Hence, though the forming operation is bending dominant, the impact of membrane effects on the forming forces is not negligible. The slight “waviness” of the curves in Fig. 8 is owed to the coarse discretization according to Table 2. This does not impede the comparison of plasticity models, but could, in principle, be

resolved by a mesh-refinement to improve the contact resolution [13].

To conclude this experiment the intensities of the membrane forces represented by  $I_N$  as a contour plot for the cp-model, the novel shell srp-model and the plate srp-model are plotted in Figs. 9, 10 and 11, respectively. Expectedly, the proposed shell srp-model matches the continuum behavior significantly better than the plate srp-model. It is also noteworthy, that the largest intensities of  $I_N$  occur at the outermost fibers before entering the roll gap. This is a well established fact in practice: Material particles moving along the curved side edges are stretched as they must travel a greater distance than particles following the shorter path in the center.

## 7 Response of a through-the-thickness element subjected to a roll forming strain history

To facilitate a comparison of the shell srp-model with Crisfield’s model in the practical scenario of roll forming, the numerical experiments on the through-the-thickness element of Sect. 4 are reconsidered, but this time the thickness element is subjected to strain histories of actual roll forming simulations. This presents an easy way to continue the validation without having to implement Crisfield’s model in the finite element framework.

For this sake, the results obtained in Sect. 6, from the reference simulations with the cp-model for the particular choice  $\rho = 0.004 \text{ m}$  are taken. More specifically, the steady

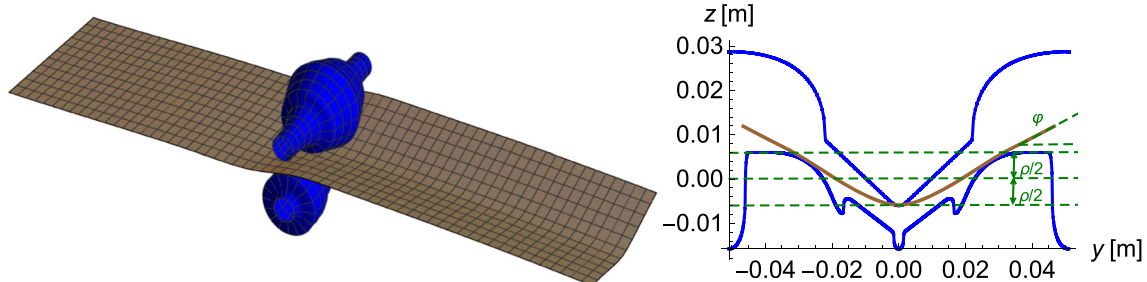


**Fig. 7** Final, steady state configuration of the roll forming experiment with one roll stand (left); annotated view of the cross section at the roll stand showing the roll-gap-reduction parameter  $\rho$  and the bending angle  $\varphi$  (right)

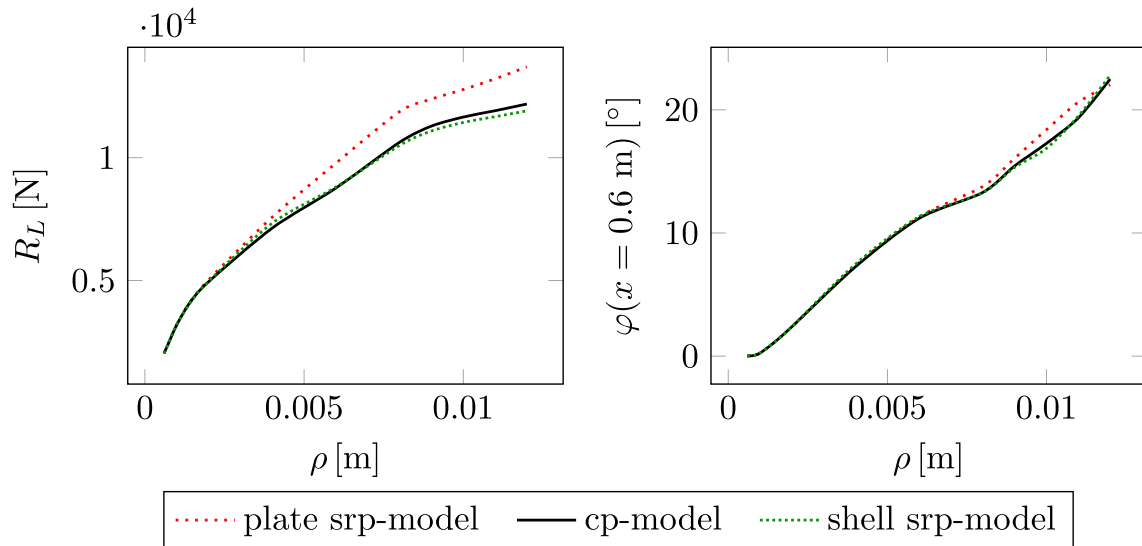


**Fig. 8** Comparison of the different plasticity models in terms of the roll force on the lower roll  $R_L$  and the bending angle  $\varphi(x = 0.6 \text{ m})$  for increasing values of the roll-gap-reduction  $\rho$

**Fig. 9** Intensities  $I_N$  of the shell as obtained for the continuum plasticity model of [13] in the steady state configuration of the roll forming experiment with one roll stand and  $\rho = 0.004\text{m}$

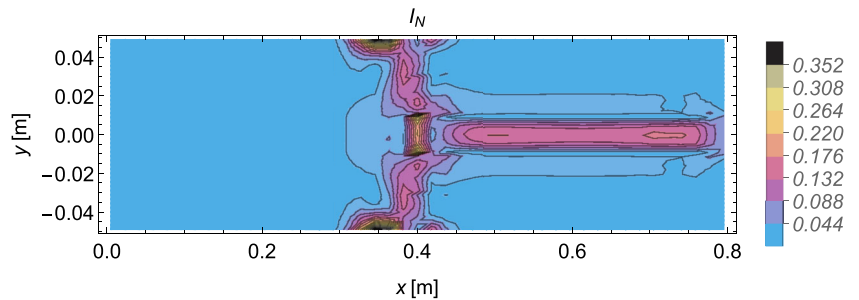


**Fig. 10** Intensities  $I_N$  of the shell as obtained for the proposed shell stress resultant plasticity model in the steady state configuration of the roll forming experiment with one roll stand and  $\rho = 0.004\text{m}$

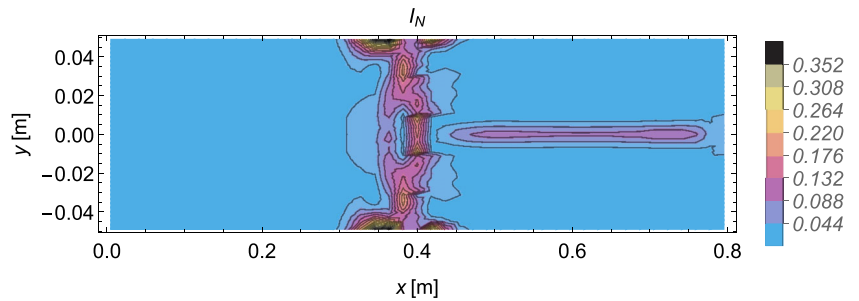
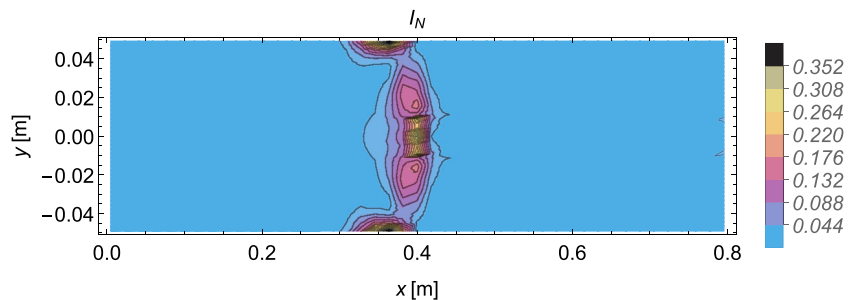


**Fig. 11** Intensities  $I_N$  of the shell as obtained for the plate stress resultant plasticity model of [12] in the steady state configuration of the roll forming experiment with one roll stand and  $\rho = 0.004\text{m}$



state strains  $\mathbf{E}$  and  $\mathbf{K}$  encountered by a material particle on its way through the control domain  $0 \leq x \leq L$  are imposed on the through-the-thickness element by means of:

$$\mathbf{E}(x(t), y^*), \quad \mathbf{K}(x(t), y^*), \quad x(t) = t/L, \quad (48)$$

where  $y^*$  is the lateral position of an axial fiber and the load-application is controlled with the pseudo-time  $0 < t \leq 1$  in resemblance of (39). The strain histories are evaluated for the outermost line of integration points at  $y^* = 0.049\text{m}$  and the innermost line at  $y^* = 0.0011\text{m}$ . A piecewise quadratic interpolation is used to obtain a smooth strain history from the discrete integration point values. The time-histories of  $I_N$  and  $I_M$  as well as the hardening functions are depicted in Figs. 12, 13 and 14.

It is important to note that the thus produced time histories for the plate srp-model, the shell srp-model and the Crisfield model are artificial to a varying degree. This is due to the fact, that the strain history of the simulation with the continuum plasticity model is imposed, which generally differs from the corresponding strain histories obtained from simulations with the stress resultant plasticity models.

From Fig. 12 it can be concluded that the shell srp-model very closely replicates the reference solution of the cp-model for the outermost fiber. The plate srp-model is equally accurate with regard to the bending invariant  $I_M$  but exhibits a strong deviation in the membrane invariant  $I_N$ . Crisfield's model produces reasonably accurate results, which are however harder to obtain numerically owing to the less favorable convergence behavior of the time integration scheme already noted in Sect. 4.

The time histories for the innermost fiber depicted in Fig. 13 show, however, significant differences between the continuum and the stress resultant plasticity models. In order to investigate this discrepancy, the time history of the dominant components of the bending moments  $M_x(t)$  and  $M_y(t)$  are presented in Fig. 15. Here, the non-monotonous characteristic of the axial bending moment  $M_x$ , which relates to the axial curvature induced by the rolls, entails a significant change of the load case that even induces reverse plasticity. The stress resultant plasticity models fail to reproduce such load histories accurately, because the employed isotropic hardening functions that govern the progression of plastic flow rest upon the assumption of a monotonously increasing loading. However, for the considered type of profile geometry these discrepancies remain confined to the proximity of the center fiber and, as depicted in Fig. 8, do not perceptively deteriorate the correspondence in terms of the primary variables of the forming process.

Finally, Fig. 14 demonstrates, that plastic flow at outer- and inner- fiber is initiated even before the sheet enters the roll gap at  $x = 0.4\text{m}$ , which is a well established observation in the engineering practice of roll forming [33, 34].

## 8 Practical example of U-shaped profile formed by three roll stands

Here, a simulation with three roll stands in which a simple U-shaped geometry with a final forming angle of  $\varphi = \pi/4$  is produced, is considered. The steady state configuration with fully closed roll gaps is depicted in Fig. 16. The simulation parameters are provided in Table 3. The edge at  $x = 0$  is again fully clamped (in- and out-of-plane) and the three roll stands are positioned at  $x_i = \{0.39, 0.78, 1.17\}\text{m}$ .

Table 4 presents the resulting forming forces  $R_{Li}$  (resultant contact forces) on the lower rolls as obtained from the stress resultant plasticity models and the relative errors  $\epsilon_{Li}$  in comparison to the continuum plasticity approach, which serves as reference solution. The shell srp-model provides highly accurate results (at significantly lower computational cost), whereas the plate srp-model significantly overestimates these forces. This inability to produce accurate forming forces is a consequence of the incomplete description of plasticity with respect to the membrane forces. On the other hand, the evolution of bending angles along the axis  $x$  as depicted in Fig. 17 shows good correspondence of all three considered models. Hence, in accordance with the observations made for the experiment with a single roll stand in Sect. 6, the estimated membrane forces have a strong influence on the required forming forces to obtain a given profile geometry.

In comparison to the cp-model the primary advantage of the shell srp-model is, that it produces practically accurate results at approximately one-fifth of the total simulation time.<sup>1</sup>

## 9 Conclusion

The proposed Kirchhoff–Love shell stress resultant plasticity model is designed for a bending dominant framework in which membrane forces remain small to moderate. The derivation rests upon a proper combination of a previously reported stress resultant plasticity model for elastic-plastic plate bending and an augmented version of the Ilyushin yield criterion proposed by Crisfield. The thus deduced stress resultant plasticity formulation presents a computationally more efficient alternative to the usually applied continuum approach with a through-the-thickness resolution of plastic states. This advantage is of crucial importance since econ-

<sup>1</sup> Reaching a quasi-steady state solution for the parameter set from Table 3 takes about 45 days for the cp-model vs. 9 days for the shell srp-model and vs. 8 days for the plate srp-model on a 6-core Intel(R) Core(TM) i7-8850H CPU at 2.60GHz. This comparison of simulation times stands regardless of the inherent inefficiency of the in-house finite element code. In the latter respect, preliminary studies show, that limited optimization measures are easily capable of reducing the simulation time with the shell srp-model to less than a day.

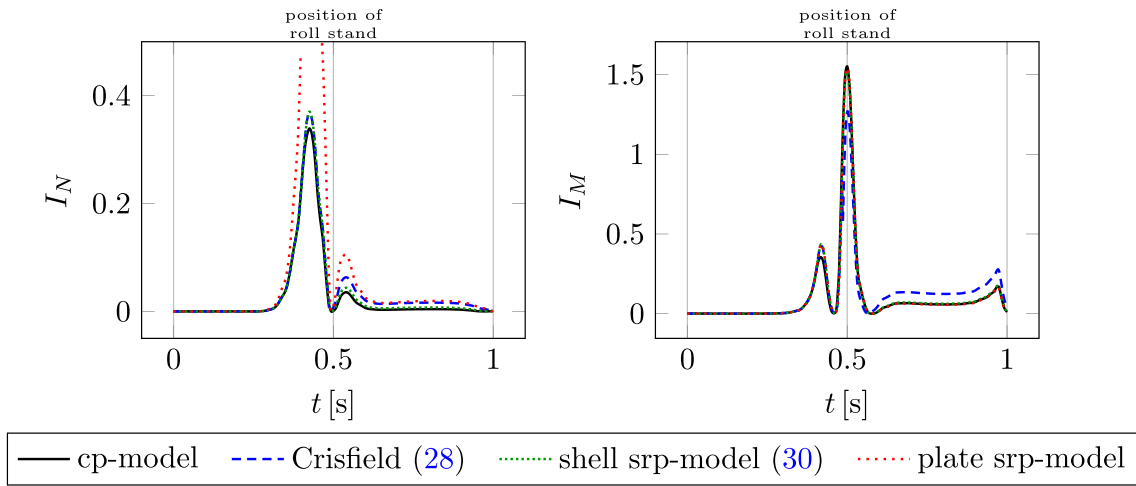


**Fig. 12** Comparison of simulation results of the through-the-thickness element between the four different plasticity models with the strain history of the outermost fiber;  $y^* = 0.049m$  and  $\rho = 0.004m$

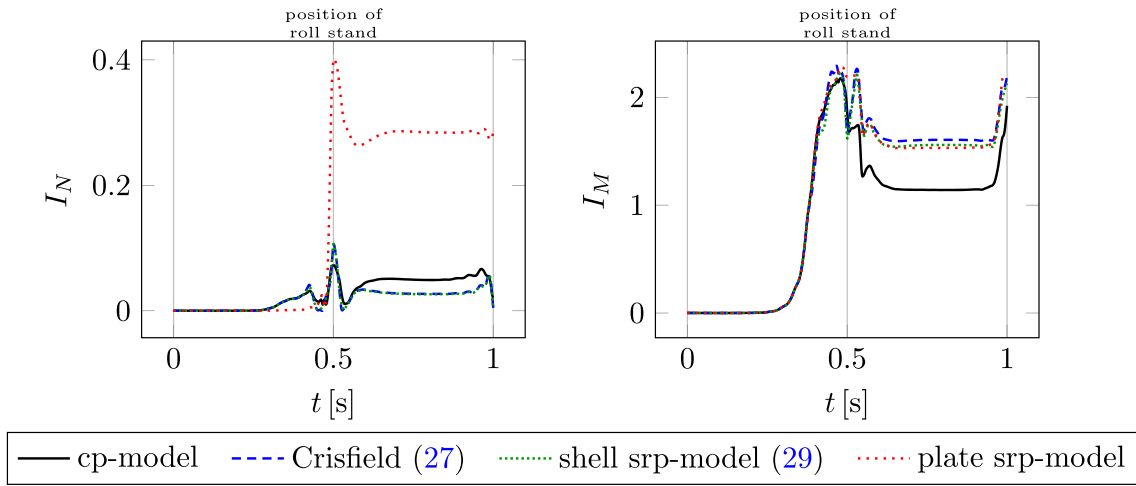


**Fig. 13** Comparison of simulation results of the through-the-thickness element between the four different plasticity models with the strain history of the innermost fiber;  $y^* = 0.0011m$  and  $\rho = 0.004m$

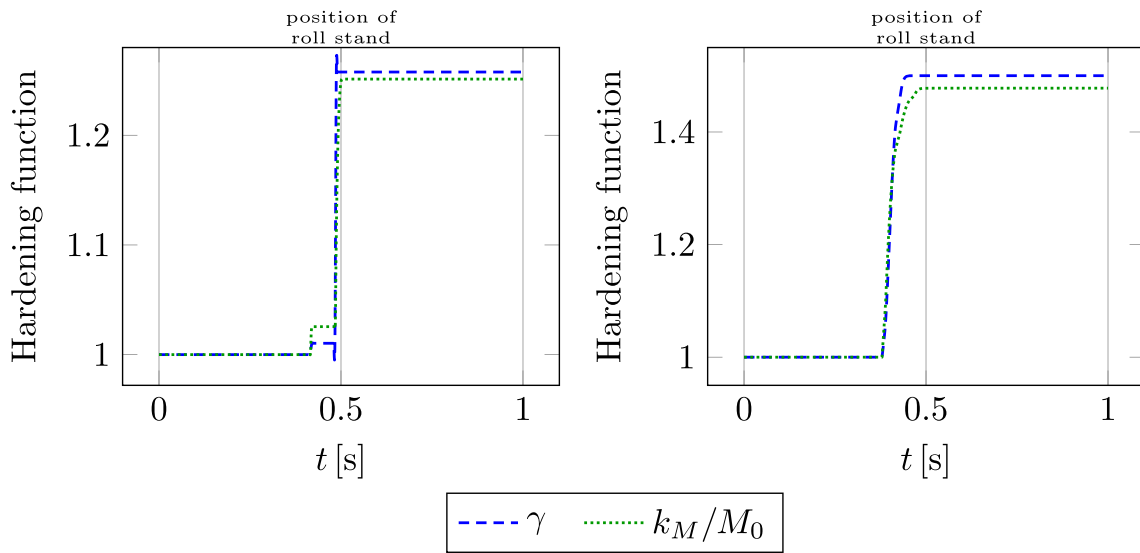


**Fig. 14** Comparison of the hardening functions for outermost fiber (left) and innermost fiber (right)

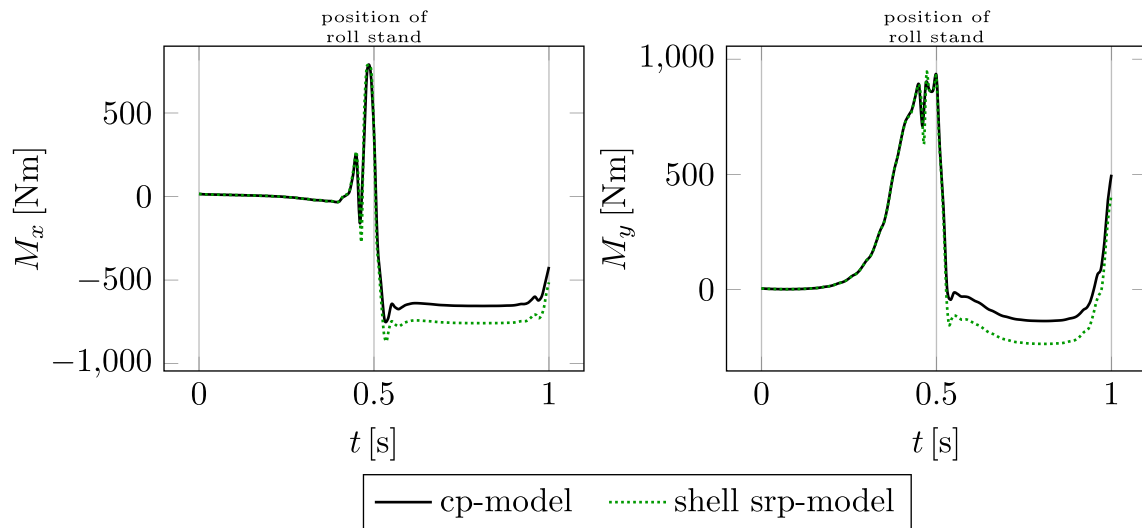


**Fig. 15** Comparison of simulation results of the bending moments of the through-the-thickness element for the innermost fiber with  $y^* = 0.0011m$  and for  $\rho = 0.004m$

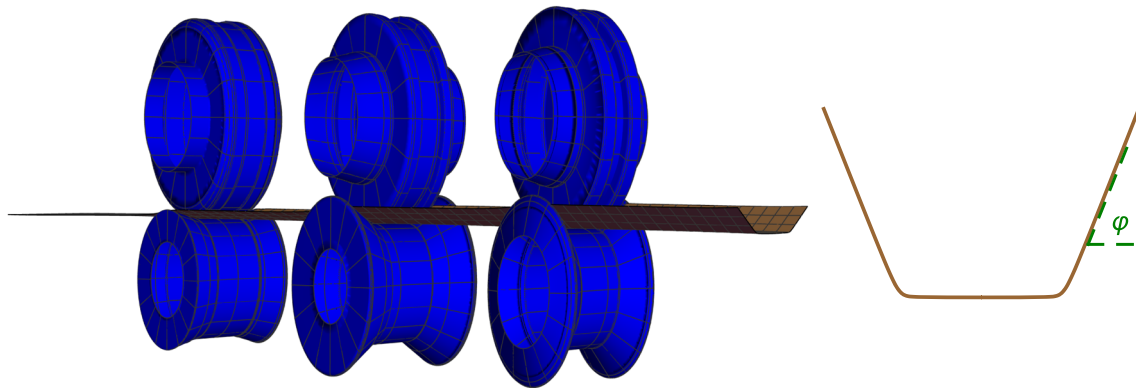


**Fig. 16** Final, steady state configuration of the roll forming experiment with three roll stands

**Table 3** Parameters of the roll forming simulation with three roll stands

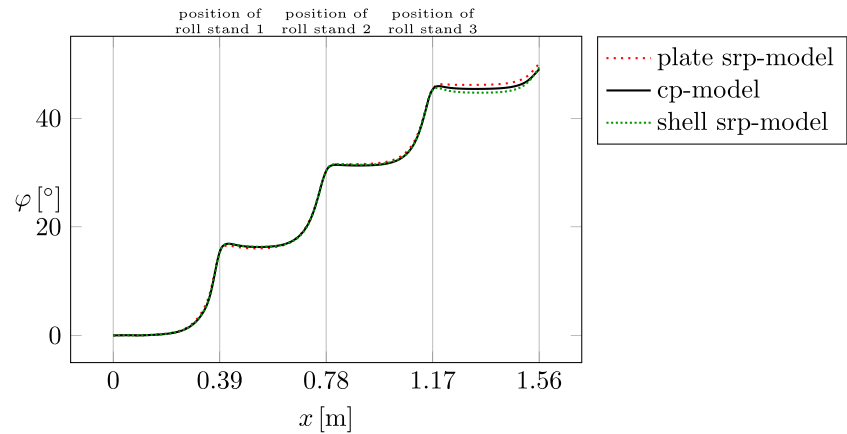
Geometry			Material			
$L$ [m]	$w$ [m]	$h$ [m]	$E$ [N/m <sup>2</sup> ]	$\nu$	$k$ [N/m <sup>2</sup> ]	
1.56	0.12	0.0015	$2.08 \times 10^{11}$	0.3	$362 \times 10^6$	
Forming		Transport		Numerical		
$\rho$ [m]	$v$ [m/s]	$\Delta t$ [s]	$N_x$	$N_y$	$N_z$	$P$ [N/m <sup>3</sup> ]
$\rho_{max}$	0.8	0.005	56	20	8	$1 \times 10^{13}$

**Table 4** Stationary forces and relative errors with respect to the continuum reference solution for the simulation with three roll stands

Model	$R_{L1}$ [N]	$R_{L2}$ [N]	$R_{L3}$ [N]	$\epsilon_{L1}$ [%]	$\epsilon_{L2}$ [%]	$\epsilon_{L3}$ [%]
cp-model	5396	7493	10710	-	-	-
shell srp-model	5480	7487	10491	1.56	-0.08	-2.05
plate srp-model	5838	10008	15607	8.19	33.57	45.72



**Fig. 17** Comparison of the resulting stationary bending angles  $\varphi(x)$  for the three different plasticity models in the simulation with three roll stands



omy of time is an important design goal when developing simulation tools for industrial applications like the here considered process of sheet metal roll forming.

The proposed model is tested in a series of experiments on a through-the-thickness element by imposing bending and membrane strain histories. Moreover, it is implemented in an existing mixed Eulerian–Lagrangian finite element scheme that is designed for the simulation of the sheet metal roll forming process. For the purpose of validation, reference solutions are obtained with the established continuum plasticity approach. In the considered scenarios, the new model surpasses the previously reported stress resultant plasticity models in terms of accuracy and computational efficiency.

Like its predecessors the model captures the evolution of plastic zones through the thickness by means of a custom isotropic hardening law. As such it is well applicable to cases that feature a monotonous increase of a given type of loading, whereas non-monotonous load histories that induce reverse plastic bending cannot be captured accurately. It is interesting to note that even in case of the roll forming process, which features a progressive bending of an initially flat metal sheet, the phenomenon of reverse plasticity may occur in certain parts of the cross section. This is due to the curvature in axial direction that the rolls impose on the sheet as it is passing through the roll gap. Future research may focus on the resolution of this persistent limitation, which nonetheless does not inhibit the usability of the proposed model as long as reverse plasticity has no dominant impact on the outcome of the forming process.

In the roll forming scenarios considered so far, which featured simulation models with one and three roll stands to produce a V-shaped and a U-shaped profile, the novel shell stress resultant plasticity model produces accurate results in terms of contact forces and bending angles when compared to reference simulations conducted with the continuum plasticity approach. In contrast to the previously reported model for elastic-plastic plate bending, the additional account for membrane effects in the plasticity model significantly improves

the estimates of the forming forces. Ultimately, the enhanced shell stress resultant plasticity model paired with the mixed Eulerian–Lagrangian finite element framework presents a major step towards a both computationally efficient and accurate simulation of the sheet metal roll forming process.

**Acknowledgements** The authors acknowledge TU Wien Bibliothek for financial support through its Open Access Funding Programme.

**Author Contributions** All authors contributed to the study conception and design. Material preparation, data collection and analysis were performed by all authors. The first draft of the manuscript was written by [Emin Kocbay] and all authors commented on previous versions of the manuscript. All authors read and approved the final manuscript.

**Funding** Open access funding provided by TU Wien (TUW). The authors declare that no funds, grants, or other support were received during the preparation of this manuscript.

## Declarations

**Competing Interests** The authors have no relevant financial or non-financial interests to disclose.

**Open Access** This article is licensed under a Creative Commons Attribution 4.0 International License, which permits use, sharing, adaptation, distribution and reproduction in any medium or format, as long as you give appropriate credit to the original author(s) and the source, provide a link to the Creative Commons licence, and indicate if changes were made. The images or other third party material in this article are included in the article's Creative Commons licence, unless indicated otherwise in a credit line to the material. If material is not included in the article's Creative Commons licence and your intended use is not permitted by statutory regulation or exceeds the permitted use, you will need to obtain permission directly from the copyright holder. To view a copy of this licence, visit <http://creativecommons.org/licenses/by/4.0/>.

## References

- Ambati M, Kiendl J, De Lorenzis L (2018) Isogeometric Kirchhoff–Love shell formulation for elasto-plasticity. *Comput Methods Appl Mech Eng* 340:320–339. <https://doi.org/10.1016/j.cma.2018.05.023>

2. Brank B, Perić D, Damjanić FB (1997) On large deformations of thin elasto-plastic shells: implementation of a finite rotation model for quadrilateral shell element. *Int J Numer Methods Eng* 40(4):689–726. [https://doi.org/10.1002/\(SICI\)1097-0207\(19970228\)40:4<689::AID-NME85>3.0.CO;2-7](https://doi.org/10.1002/(SICI)1097-0207(19970228)40:4<689::AID-NME85>3.0.CO;2-7)
3. Liguori FS, Madeo A, Garcea G (2022) A dual decomposition of the closest point projection in incremental elasto-plasticity using a mixed shell finite element. *Int J Numer Methods Eng* 123(24):6243–6266. <https://doi.org/10.1002/nme.7112>
4. Alaydin MD, Benson DJ, Bazilevs Y (2021) An updated Lagrangian framework for isogeometric Kirchhoff-Love thin-shell analysis. *Comput Methods Appl Mech Eng* 384. <https://doi.org/10.1016/j.cma.2021.113977>
5. Li J, Liu C, Hu H, et al (2021) Analysis of elasto-plastic thin-shell structures using layered plastic modeling and absolute nodal coordinate formulation. *Nonlinear Dynamics* 105(4). <https://doi.org/10.1007/s11071-021-06766-9>
6. Ilyushin A (1948) *Plasticity*. GITL, Moscow, Leningrad ((in Russian))
7. Bieniek MP, Funaro JR (1976) *Elasto-plastic behavior of plates and shells*. Tech. rep, Weidlinger Associates New York
8. Crisfield M (1981) Finite element analysis for combined material and geometric nonlinearities. In: *Nonlinear finite element analysis in structural mechanics*. Springer, pp 325–338
9. Zeng Q, Combescure A, Arnaudeau F (2001) An efficient plasticity algorithm for shell elements application to metal forming simulation. *Comput Struct* 79(16):1525–1540. [https://doi.org/10.1016/S0045-7949\(01\)00032-3](https://doi.org/10.1016/S0045-7949(01)00032-3)
10. Dujc J, Brank B (2008) On stress resultant plasticity and viscoplasticity for metal plates. *Finite Elem Anal Des* 44(4):174–185. <https://doi.org/10.1016/j.finel.2007.11.011>
11. Dujc J, Brank B (2012) Stress resultant plasticity for shells revisited. *Comput Methods Appl Mech Eng* 247–248:146–165. <https://doi.org/10.1016/j.cma.2012.07.012>
12. Kochbay E, Vetyukov Y (2021) Stress resultant plasticity for plate bending in the context of roll forming of sheet metal. *Int J Numer Methods Eng* 122(18):5144–5168. <https://doi.org/10.1002/nme.6760>
13. Kochbay E, Scheidl J, Riegler F et al (2023) Mixed Eulerian-Lagrangian modeling of sheet metal roll forming. *Thin-Walled Structures* 186:110662. <https://doi.org/10.1016/j.tws.2023.110662>
14. Heislitz F, Livatyali H, Ahmetoglu MA, et al (1996) Simulation of roll forming process with the 3-D FEM code PAM-STAMP. *J Mater Process Technol* 59(1):59–67. [https://doi.org/10.1016/0924-0136\(96\)02287-X](https://doi.org/10.1016/0924-0136(96)02287-X), selected Papers on Metal Forming and Machining
15. Bui Q, Ponthot J (2008) Numerical simulation of cold roll-forming processes. *J Mater Process Technol* 202(1):275–282. <https://doi.org/10.1016/j.jmatprotec.2007.08.073>
16. Vetyukov Y, Gruber P, Krommer M (2016) Nonlinear model of an axially moving plate in a mixed Eulerian-Lagrangian framework. *Acta Mechanica* 227:2831–2842. <https://doi.org/10.1007/s00707-016-1651-0>
17. Vetyukov Y, Gruber P, Krommer M et al (2017) Mixed Eulerian-Lagrangian description in materials processing: deformation of a metal sheet in a rolling mill. *Int J Numer Methods Eng* 109(10):1371–1390. <https://doi.org/10.1002/nme.5314>
18. Donea J, Huerta A, Ponthot JP, et al (2004) Arbitrary Lagrangian-Eulerian methods. In: Stein E, de Borst R, Hughes T (eds) *Encyclopedia of computational mechanics*, vol 1: Fundamentals. Wiley, Ltd, chap 14
19. Crutzen Y, Boman R, Papeleux L, et al (2016) Lagrangian and arbitrary Lagrangian Eulerian simulations of complex roll-forming processes. *Comptes Rendus Mécanique* 344(4):251–266. <https://doi.org/10.1016/j.crme.2016.02.005>, computational simulation of manufacturing processes
20. Han S (2023) Configurational forces and ALE formulation for geometrically exact, sliding shells in non-material domains. *Comput Methods Appl Mech Eng* 412:116106. <https://doi.org/10.1016/j.cma.2023.116106>
21. Scheidl J, Vetyukov Y (2020) Steady motion of a slack belt drive: dynamics of a beam in frictional contact with rotating pulleys. *J Appl Mech* 87(12). <https://doi.org/10.1115/1.4048317>, 121011
22. Scheidl J, Vetyukov Y, Schmidrathner C et al (2021) Mixed Eulerian-Lagrangian shell model for lateral run-off in a steel belt drive and its experimental validation. *Int J Mech Sci* 204:106572. <https://doi.org/10.1016/j.ijmecsci.2021.106572>
23. Eliseev VV, Vetyukov YM (2010) Finite deformation of thin shells in the context of analytical mechanics of material surfaces. *Acta Mechanica* 209(1–2):43. <https://doi.org/10.1007/s00707-009-0154-7>
24. Vetyukov Y (2014) *Nonlinear mechanics of thin-walled structures: asymptotics, direct approach and numerical analysis*. Springer Sci Bus Media
25. Lubliner J (2008) *Plasticity theory*. Dover Publications, Inc
26. Hu Q, Li X, Chen J (2018) On the calculation of plastic strain by simple method under non-associated flow rule. *Eur J Mech-A/Solids* 67:45–57. <https://doi.org/10.1016/j.euromechsol.2017.08.017>
27. Crisfield M, Peng X (1992) Efficient nonlinear shell formulations with large rotations and plasticity. DRJ Owen et al *Computational plasticity: models, software and applications*, Part 1:1979–1997
28. Mohammed AK, Skallerud B, Amdahl J (2001) Simplified stress resultants plasticity on a geometrically nonlinear constant stress shell element. *Comput Struct* 79(18):1723–1734. [https://doi.org/10.1016/S0045-7949\(01\)00095-5](https://doi.org/10.1016/S0045-7949(01)00095-5)
29. Bogner FK, Fox RL, Schmit LA (1965) The generation of interelement compatible stiffness and mass matrices by the use of interpolation formulae. In: *Proc. Conf. Matrix Methods in Struct. Mech.*, Airforce Inst. Of Tech., Wright Patterson AF Base, Ohio
30. Eisenträger S, Kiendl J, Michaloudis G et al (2022) Stability analysis of plates using cut Bogner-Fox-Schmit elements. *Comput Struct* 270:106854. <https://doi.org/10.1016/j.compstruc.2022.106854>
31. Mueller C, Gu X, Baeumer L, et al (2014) Influence of friction on the loads in a roll forming simulation with compliant rolls. In: *Material forming ESAFORM 2014*, key engineering materials, vol 611. Trans Tech Publications Ltd, pp 436–443. <https://doi.org/10.4028/www.scientific.net/KEM.611-612.436>
32. Paralikas J, Salonitis K, Chryssolouris G (2009) Investigation of the effects of main roll-forming process parameters on quality for a V-section profile from AHSS. *Int J Adv Manuf Technol* 44(3):223–237. <https://doi.org/10.1007/s00170-008-1822-9>
33. Bhattacharyya D, Smith P, Yee C et al (1984) The prediction of deformation length in cold roll-forming. *J Mech Work Technol* 9(2):181–191. [https://doi.org/10.1016/0378-3804\(84\)90004-4](https://doi.org/10.1016/0378-3804(84)90004-4)
34. Lindgren M (2007) An improved model for the longitudinal peak strain in the flange of a roll formed U-channel developed by FE-analyses. *Steel Res Int* 78(1):82–87. <https://doi.org/10.1002/srin.200705863>

**Publisher's Note** Springer Nature remains neutral with regard to jurisdictional claims in published maps and institutional affiliations.